



Cite this: *J. Mater. Chem. C*, 2015,  
3, 7677

## Co<sup>2+</sup>/Co<sup>3+</sup> ratio dependence of electromagnetic wave absorption in hierarchical NiCo<sub>2</sub>O<sub>4</sub>–CoNiO<sub>2</sub> hybrids†

Hongjing Wu,<sup>\*ab</sup> Guanglei Wu,<sup>ac</sup> Yanyan Ren,<sup>a</sup> Le Yang,<sup>a</sup> Liuding Wang<sup>a</sup> and Xinghua Li<sup>d</sup>

Amorphous hierarchical NiCo<sub>2</sub>O<sub>4</sub>–CoNiO<sub>2</sub> hybrids have been successfully fabricated via a facile one-pot hydrothermal route, followed by morphological conversion into urchin-like structured NiCo<sub>2</sub>O<sub>4</sub>–CoNiO<sub>2</sub> nanorods and irregular-shaped hierarchical NiCo<sub>2</sub>O<sub>4</sub>–CoNiO<sub>2</sub> polyhedral nanocrystals through air-annealing treatment at 450 °C and 650 °C, respectively. The phase structure, morphology and chemical composition have been characterized in detail. Calcined hierarchical NiCo<sub>2</sub>O<sub>4</sub>–CoNiO<sub>2</sub> hybrids show improved microwave absorption properties, which are ascribed to the synergistic effect of dielectric CoNiO<sub>2</sub> and NiCo<sub>2</sub>O<sub>4</sub> phases. In particular, the calcined hierarchical NiCo<sub>2</sub>O<sub>4</sub>–CoNiO<sub>2</sub> hybrids at 450 °C exhibit significant enhancement in complex permittivity with respect to others due to their remarkable dipole polarization and interfacial polarization. The maximum reflection loss (RL) of the calcined hierarchical NiCo<sub>2</sub>O<sub>4</sub>–CoNiO<sub>2</sub> hybrids at 450 °C reaches –42.13 dB at 11.84 GHz with a matching thickness of 1.55 mm, and a relatively broad absorption bandwidth (RL ≤ –10 dB) in the 13.12–17.04 GHz range. Very interestingly, the electromagnetic (EM) wave absorption performance of the hierarchical NiCo<sub>2</sub>O<sub>4</sub>–CoNiO<sub>2</sub> hybrids shows dependence on the Co<sup>2+</sup>/Co<sup>3+</sup> ratio. The calcined NiCo<sub>2</sub>O<sub>4</sub>–CoNiO<sub>2</sub> hybrids at 450 °C of the most defect concentration possess the best EM wave absorption ability among all the samples. The results suggest that appropriate interactions between the building blocks in hybrids can guide us to design and fabricate highly efficient EM wave absorption materials.

Received 11th June 2015,  
Accepted 2nd July 2015

DOI: 10.1039/c5tc01716e

[www.rsc.org/MaterialsC](http://www.rsc.org/MaterialsC)

## 1. Introduction

Microwave absorbing materials (MAMs) working at a frequency of 2–18 GHz have attracted increasing attention due to their prospective potential applications in industry, civil, commercial, and military technologies. Various absorbers with matching complex permittivity and permeability, including ferrites, magnetic metallic fillers, nanosized particles, carbon nanomaterials, conductive fibers, frequency selective surfaces, and even meta-materials, have been developed to design MAMs during the last few decades.<sup>1–25</sup> MAMs can absorb electromagnetic (EM)

waves effectively and convert energy into thermal energy or dissipate the EM waves by interference. The effectiveness of a MAM is mainly dependent on its EM characteristics, *i.e.*, complex permittivity and permeability, so the key point in obtaining thin-layer broad-band MAMs is the control of the EM properties of such MAMs.

As one of the most important magnetic nanomaterials, soft magnet ferrite (MFe<sub>2</sub>O<sub>4</sub>) has large saturation magnetization, obvious Snoek's limit, great coercivity, excellent chemical stability, and corrosion resistance, which results in high complex permeability values at wide frequency ranges.<sup>25,26</sup> Recently, in order to effectively improve the microwave absorption of graphene (GP)-filled composites, attention has been directed toward adding magnetic ferrite materials such as CoFe<sub>2</sub>O<sub>4</sub>, MnFe<sub>2</sub>O<sub>4</sub> or NiFe<sub>2</sub>O<sub>4</sub> particles to GP-filled composites to improve their complex permeability.<sup>3,27,28</sup> For example, a minimum reflection loss (RL) of –18.5 dB was obtained at 12.9 GHz for the CoFe<sub>2</sub>O<sub>4</sub> hollow sphere/GP composites with a thickness of 2.00 mm, and the effective absorption frequency of –10 dB ranged from 11.3 to 15.0 GHz.<sup>27</sup> The minimum RL of reduced graphene oxide (RGO)/MnFe<sub>2</sub>O<sub>4</sub>/PVDF composites could reach –29.0 dB at 9.2 GHz, and the bandwidth of frequency <–10 dB

<sup>a</sup> Department of Applied Physics, Northwestern Polytechnical University, Xi'an, P. R. China. E-mail: wuhongjing@mail.nwpu.edu.cn; Fax: +86-29-8843-1664; Tel: +86-29-8843-1664

<sup>b</sup> NPU-UM II joint Laboratory of Soft Matter, School of Science, Northwestern Polytechnical University, Xi'an, P. R. China

<sup>c</sup> Center of Nanomaterials for Renewable Energy (CNRE), State Key Laboratory of Electrical Insulation and Power Equipment, School of Electrical Engineering, Xi'an Jiaotong University, Xi'an, P. R. China

<sup>d</sup> School of Physics, Northwest University, Xi'an, P. R. China

† Electronic supplementary information (ESI) available. See DOI: 10.1039/c5tc01716e

was from 8.00 to 12.88 GHz.<sup>3</sup> NiFe<sub>2</sub>O<sub>4</sub> nanorod-graphene composites were synthesized by a facile one-step hydrothermal process in the presence of an ionic liquid and the result indicated that the RL below -10 dB ranged from 13.6 to 18 GHz with a thickness of 2.00 mm.<sup>28</sup> These experimental results show that the enhanced microwave absorption of GP/ferrite particle-filled composites are mainly due to the increased magnetic loss and the unique microstructure as a result of the presence of magnetic particles. Hence, excellent EM wave absorption properties of the composites can be realized by reasonably incorporating magnetic ferrite particles with different EM properties, particle sizes, and morphologies.

Although the complex permeability can be tailored by adding magnetic ferrite particles to improve the microwave absorption of the composites, it is still a challenge to design and fabricate composites to satisfy the demand of ideal MAMs. For example, the complex permeability is increased as the magnetic ferrite (MFe<sub>2</sub>O<sub>4</sub>) particles are incorporated into the composites, but the values of the complex permeability is still lower compared with the complex permittivity, which results in such MAMs exhibiting no visible enhancement of RL. On the other hand, some negative values of  $\mu''$  of the composites also appear in the measured frequency range,<sup>19,29-32</sup> and few studies can give a detailed discussion on the mechanism of such a unique phenomenon. If the absolute values of  $\mu''$  of some reported composites are small in the measured frequency range ( $\leq 0.1$ ), the negative  $\mu''$  may result from a problem with the calibration procedures of the microwave test setup. Therefore, we cannot use the complex permeability, *i.e.*, the negative value of  $\mu''$  of the composites, to calculate the magnetic loss and RL of such MAMs.

One feasible approach to overcome these drawbacks is the design and synthesis of novel hierarchical spinel nanocrystals with reasonable composition, morphology, microstructure, and architecture on the nanoscale, but there has been few reports about the EM and microwave-absorbing properties of novel hierarchical magnetic spinel nanocrystals.<sup>25,26</sup> In particular, hierarchical structures, which assembled by nanoscale primary building blocks (*e.g.*, nanoparticles, nanorods, and nanosheets) with porous characteristics, have drawn special interest.<sup>33</sup> It is anticipated that such hierarchical structures not only inherit the advantages from the single components but also arise novel properties due to the synergistic interactions between the nano building blocks.<sup>34,35</sup>

To date, spinel ferrites with various compositions have been already synthesized and used as MAMs.<sup>25,28</sup> However, as an important spinel structure, nickel cobalt oxide (*i.e.*, NiCo<sub>2</sub>O<sub>4</sub>) was mainly used in the electrochemistry field,<sup>33,34</sup> and to the best of our knowledge, there has been few reports about the microwave absorbing property of NiCo<sub>2</sub>O<sub>4</sub> so far.<sup>36</sup> Furthermore, little attention has been paid to nickel cobalt oxides with compositions other than NiCo<sub>2</sub>O<sub>4</sub> (*i.e.*, CoNiO<sub>2</sub>) for the applications as supercapacitor electrodes or MAMs. In order to achieve a novel absorption property, many efforts have been devoted to combine two or more than two kinds of functional materials to adjust the EM parameters for achieving a desired RL. Inspired by this thought, in this work, we reported the facile synthesis of novel hierarchical NiCo<sub>2</sub>O<sub>4</sub>-CoNiO<sub>2</sub> hybrids through a one-step

hydrothermal route without a complex process, and used these hybrid nanostructures for microwave absorption. The crystalline structure, morphology, and microwave absorption of these materials were investigated in detail. Our experimental method provides a facile and reliable route for the preparation of novel hierarchical NiCo<sub>2</sub>O<sub>4</sub>-CoNiO<sub>2</sub> hybrids, which could have important applications in modern science and technology due to their good mechanical and chemical stability. It could also be a general approach for the large-scale of novel hierarchical spinel hybrids of a wide range of materials.

## 2. Experimental section

### 2.1. Materials and sample preparation

D-Glucose monohydrate purchased from National Reagent Corp. (Shanghai, China) was used as a carbon source to guide the synthesis of a core-shell solid sphere precursor.<sup>37-39</sup> Cobalt(II) nitrate hexahydrate (Co(NO<sub>3</sub>)<sub>2</sub>·6H<sub>2</sub>O), nickel(II) nitrate hexahydrate (Ni(NO<sub>3</sub>)<sub>2</sub>·6H<sub>2</sub>O), and urea (CO(NH<sub>2</sub>)<sub>2</sub>) were obtained from Tianjin Kemiou Chemical Reagent Corp. (Tianjin, China).

The hierarchical NiCo<sub>2</sub>O<sub>4</sub>-CoNiO<sub>2</sub> hybrids were prepared by the following one-pot process similar to our previous reports.<sup>37-39</sup> Briefly, D-glucose, a metal source and urea were co-dissolved in 50 ml distilled water. The molar ratio of D-glucose (0.01 mol), dissolved metal (0.02 mol, a molar ratio of Ni(NO<sub>3</sub>)<sub>2</sub> and Co(NO<sub>3</sub>)<sub>2</sub> = 1 : 1), and urea (0.02 mol) was controlled to a value of 1 : 2 : 2. After stirring for 0.5 h, the derived solution was transferred into a 100 ml capacity Teflon-lined stainless-steel autoclave followed by hydrothermal treatment at 180 °C for 20 h. The obtained products were washed and filtered off several times using distilled water and absolute ethanol successively, and finally dried at 80 °C under vacuum overnight. After synthesis, the products were calcined at 450 °C or 650 °C in air for 3 h with a heating rate of 2 °C min<sup>-1</sup> to obtain hierarchical NiCo<sub>2</sub>O<sub>4</sub>-CoNiO<sub>2</sub> hybrids.

### 2.2. Characterization

X-ray diffraction (XRD) analysis was performed on a Rigaku D/Max 2500 equipment with Cu K $\alpha$  radiation operated at 40 kV and 40 mA. The particle size and morphology were visualized by using a FEI Quanta 600 FEG scanning electronic microscope (SEM) and a FEI Tecnai G<sup>2</sup> F20 S-TWIN transmission electron microscope (TEM), and an energy-dispersive X-ray spectroscopy (EDS) attachment was used to obtain the surface element composition of synthesized samples. TEM samples were treated by sonicating in absolute ethanol for several minutes and then a few drops of the resulting suspension were deposited onto a holey-carbon film supported in a copper grid, which was dried naturally. The surface area was calculated using the Brunauer-Emmett-Teller (BET) method based on the adsorption data. Raman spectra were obtained on a Nicolet Almega spectrometer. Thermogravimetric analysis (TGA) was carried out with a temperature ramp of 10 °C min<sup>-1</sup>. The chemical states were investigated by X-ray photoelectron spectroscopy (XPS, ESCA PHI 5400) using a monochromatic Mg K $\alpha$  X-ray source (1253.6 eV).

Curve fitting was carried out using Shirley function for background correction. An asymmetric Gaussian–Lorentzian line-shape was used to fit the asymmetric photoelectron bands while a Gaussian–Lorentzian line-shape was used to fit the symmetric bands. Photoelectron bands were peak-fitted using a non-linear least-squares optimization routine with software provided by the instrument manufacturer. The magnetic properties of the products were studied by using a vibrating sample magnetometer (VSM, Lake shore 7, 304).

### 2.3. Electromagnetic measurements

The microwave absorption properties of hierarchical  $\text{NiCo}_2\text{O}_4$ – $\text{CoNiO}_2$  hybrids were investigated through a network analyzer (Agilent Technologies E8363B) in the frequency range of 2–18 GHz. The composites for microwave absorption measurement were fabricated by mixing paraffin wax with 50 wt% sample powder and pressed into a toroid shape ( $\varphi_{\text{out}} = 7.00$  mm,  $\varphi_{\text{in}} = 3.04$  mm). The complex permittivity and permeability were computed from the experimental scattering parameters through the standard Nicholson–Ross and Weir theoretical calculations.

## 3. Results and discussion

The phase structures of synthesized  $\text{NiCo}_2\text{O}_4$ – $\text{CoNiO}_2$  hybrids were measured by XRD, as displayed in Fig. 1. For calcined  $\text{NiCo}_2\text{O}_4$ – $\text{CoNiO}_2$  hybrids, the positions and relative intensities of all the diffraction peaks are consistent with the standard XRD patterns for the cubic spinel structure of bulk  $\text{NiCo}_2\text{O}_4$  (JCPDS No. 20-0781) and the cubic face-center structure of  $\text{CoNiO}_2$  (JCPDS No. 10-0188). The broadening diffraction peaks of the calcined sample at 450 °C are due to the small size effect of hierarchical  $\text{NiCo}_2\text{O}_4$ – $\text{CoNiO}_2$  nanocrystals. After annealing treatment at 650 °C, the XRD pattern of the sample shows obvious enhancement of characteristic peaks for hierarchical  $\text{NiCo}_2\text{O}_4$ – $\text{CoNiO}_2$  hybrids, indicating the agglomeration of hierarchical  $\text{NiCo}_2\text{O}_4$ – $\text{CoNiO}_2$  nanocrystals. Particularly, the absence

of characteristic peaks assigned to crystalline  $\text{NiCo}_2\text{O}_4$ – $\text{CoNiO}_2$  hybrids in uncalcined sample implies the amorphous nature of these components.

The morphologies and microstructures of hierarchical  $\text{NiCo}_2\text{O}_4$ – $\text{CoNiO}_2$  hybrids were further characterized by using scanning electron microscopy (SEM) and transmission electron microscopy (TEM). Fig. 2a, b, e, f, i and j display the SEM images of uncalcined and calcined  $\text{NiCo}_2\text{O}_4$ – $\text{CoNiO}_2$  hybrids at 450 °C and 650 °C, respectively. As shown in Fig. 2a, the uncalcined  $\text{NiCo}_2\text{O}_4$ – $\text{CoNiO}_2$  hybrid shows an uniform microsphere structure with an average diameter of ~1–2 μm. The high-magnification image of the microspheres shown in Fig. 2b indicates that the uncalcined  $\text{NiCo}_2\text{O}_4$ – $\text{CoNiO}_2$  hybrids are entirely wrapped by an amorphous  $\text{NiCo}_2\text{O}_4$ – $\text{CoNiO}_2$  hybrid layer, and the adjacent spheres are connected by the wrinkled amorphous layer. The TEM images (Fig. 2c and d) provide further insight into the detailed structure, showing that the amorphous layer thickness of the microspheres is approximately 300 nm. The amorphous hierarchical  $\text{NiCo}_2\text{O}_4$ – $\text{CoNiO}_2$  hybrid layer adhered to the microspheres can be observed in the magnified image (Fig. 2d).

After calcination at 450 °C, the amorphous hierarchical  $\text{NiCo}_2\text{O}_4$ – $\text{CoNiO}_2$  hybrid layer was transformed to a highly crystalline urchin-like structure with an average diameter of ~1–2 μm (Fig. 2e). A thin and wrinkled hierarchical  $\text{NiCo}_2\text{O}_4$ – $\text{CoNiO}_2$  hybrid layer (Fig. 2f) appears and is almost bright under SEM observation, indicating that the structure has sharp and striking morphology which is beneficial for secondary electron images. The representative TEM images of the crystalline  $\text{NiCo}_2\text{O}_4$ – $\text{CoNiO}_2$  hybrids are shown in Fig. 2g and h. An urchin-like structured  $\text{NiCo}_2\text{O}_4$ – $\text{CoNiO}_2$  hybrid is obtained. The uniform microsphere is constructed by a large number of small nanorods radially-grown from the center, and the typical diameter and length of these nanorods are ~10–20 nm and ~200–300 nm, respectively. Fig. 2h is the HR-TEM image of the nanorod from Fig. 2g. The clear lattice fringes with a *d*-spacing of 0.24 nm, 0.45 nm and 0.28 nm can be well indexed to the (111) plane of cubic  $\text{CoNiO}_2$  as well as the (111) and (220) planes of cubic  $\text{NiCo}_2\text{O}_4$ , respectively. These results further confirm that urchin-like spheres are composed of hierarchical  $\text{NiCo}_2\text{O}_4$ – $\text{CoNiO}_2$  hybrids.

For calcined  $\text{NiCo}_2\text{O}_4$ – $\text{CoNiO}_2$  hybrids at 650 °C, irregular-shaped hierarchical  $\text{NiCo}_2\text{O}_4$ – $\text{CoNiO}_2$  hybrids with a size of 1–2 μm are clearly observed (Fig. 2i and j). Moreover, the hybrids are composed of  $\text{NiCo}_2\text{O}_4$ – $\text{CoNiO}_2$  polyhedral nanocrystals. The magnified SEM image shows that  $\text{NiCo}_2\text{O}_4$ – $\text{CoNiO}_2$  nanocrystals have a well-defined polyhedral shape with sharp edges and a smooth surface (Fig. 2j, inset). For a better visualization of the polyhedral shape, Fig. 2k and l gives the TEM images of hierarchical  $\text{NiCo}_2\text{O}_4$ – $\text{CoNiO}_2$  hybrids. The  $\text{NiCo}_2\text{O}_4$ – $\text{CoNiO}_2$  nanocrystals are aggregated with an average size of ~10–30 nm to form a nearly hollow sphere (Fig. 2k). The lattice distance of  $\text{NiCo}_2\text{O}_4$ – $\text{CoNiO}_2$  polyhedral nanocrystals in hierarchical  $\text{NiCo}_2\text{O}_4$ – $\text{CoNiO}_2$  hybrids is measured to be 0.23 nm and 0.47 nm (Fig. 2l), which can be indexed to the (111) planes of cubic  $\text{CoNiO}_2$  and  $\text{NiCo}_2\text{O}_4$ . These results reveal that the synthetic method developed in this work could prepare high-quality

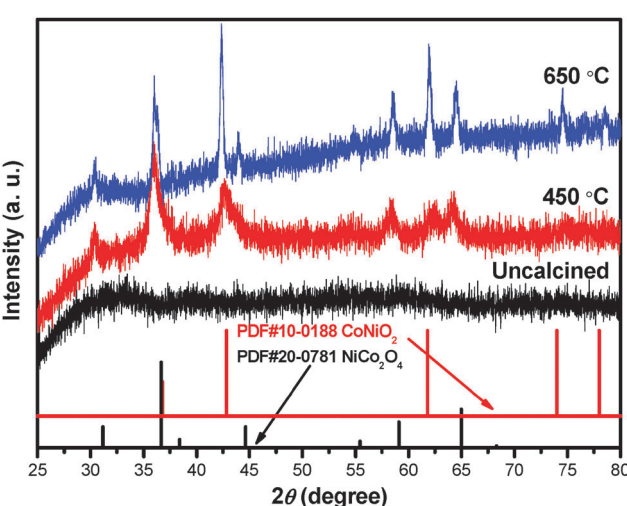
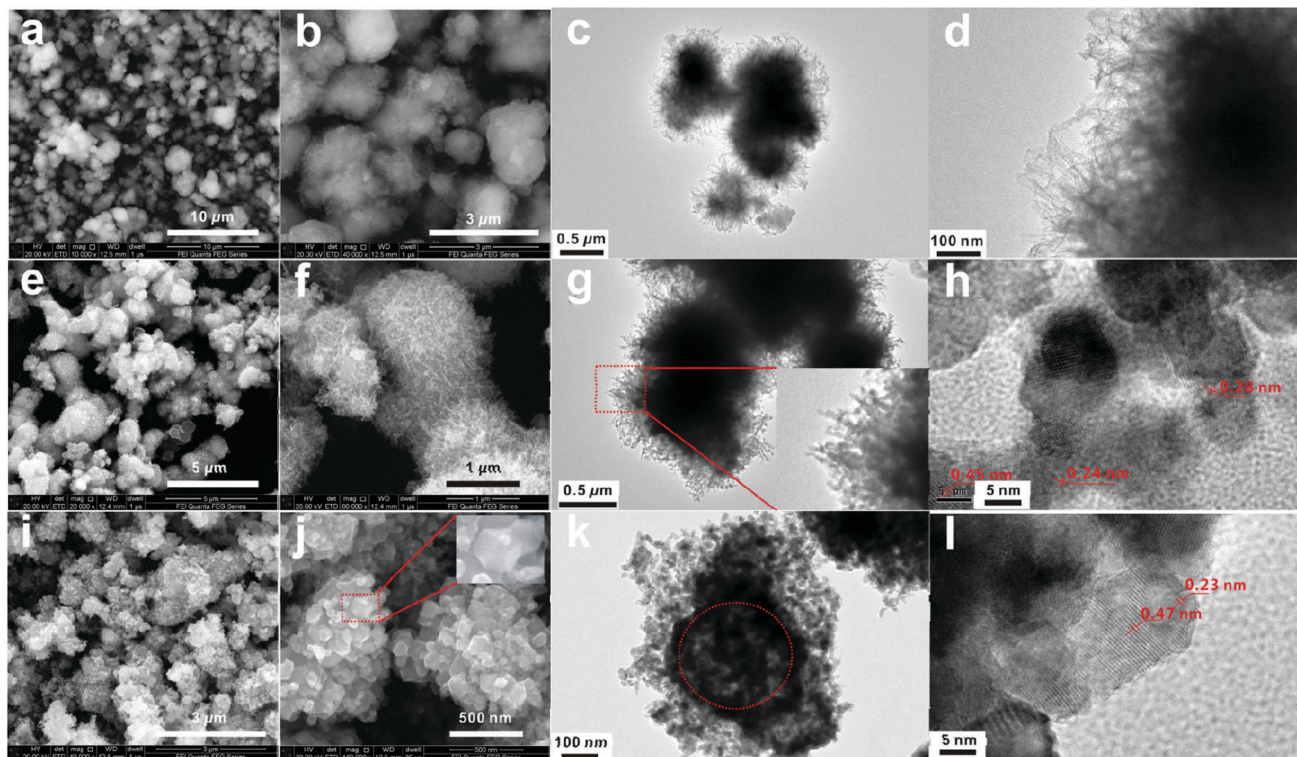


Fig. 1 XRD patterns of hierarchical  $\text{NiCo}_2\text{O}_4$ – $\text{CoNiO}_2$  hybrids.



**Fig. 2** SEM and FE-SEM images of (a and b) uncalcined sample, (e and f) calcined sample at 450 °C, and (i and j) calcined sample at 650 °C. Inset of image (j) shows the enlarged image of a single  $\text{NiCo}_2\text{O}_4$ – $\text{CoNiO}_2$  polyhedral nanocrystal. TEM and HR-TEM images of (c and d) uncalcined sample, (g and h) calcined sample at 450 °C, and (k and l) calcined sample at 650 °C. Inset of image (g) shows enlarged image of  $\text{NiCo}_2\text{O}_4$ – $\text{CoNiO}_2$  nanorods.

hierarchical  $\text{NiCo}_2\text{O}_4$ – $\text{CoNiO}_2$  hybrids composed of well-defined small nanorods and polyhedral nanocrystals. It could be noticed that the hierarchical  $\text{NiCo}_2\text{O}_4$ – $\text{CoNiO}_2$  hybrids composed of well-defined small nanorods have isotropic crystal symmetry like isotropic antennas, which may play an important role in the attenuation of the microwave.

The specific surface areas and porous nature of hierarchical  $\text{NiCo}_2\text{O}_4$ – $\text{CoNiO}_2$  hybrids were determined by measuring nitrogen adsorption–desorption isotherms at 77 K (Fig. 3). The  $\text{N}_2$  sorption isotherms of the uncalcined sample exhibit type IV isotherms with a distinct hysteresis loop in the  $P/P_0$  range of 0–1.0, typical mesoporous materials. Moreover, the pore size shows a relatively uniform distribution at 2.40 nm, illustrating superior mesoporous nanostructures. The specific surface area, mesopore volume, and average pore diameter are  $154.84 \text{ m}^2 \text{ g}^{-1}$ ,  $0.31 \text{ cm}^3 \text{ g}^{-1}$ , 8.32 nm, respectively, indicating a high surface area and porosity of the materials, which is much higher than those ( $36.84 \text{ m}^2 \text{ g}^{-1}$ ,  $0.20 \text{ cm}^3 \text{ g}^{-1}$ , 3.30 nm and  $23.47 \text{ m}^2 \text{ g}^{-1}$ ,  $0.10 \text{ cm}^3 \text{ g}^{-1}$ , 4.33 nm) of the calcined samples at 450 °C and 650 °C. Note that both highly porous structure and large surface area are beneficial to the performance of microwave absorbing materials. The incident microwaves entering the materials are reflected and scattered many times between the hierarchical structures and cannot escape from the limited space until they are completely absorbed (Table 1).

Phase changes of spinel structures are promised to have a great impact on the EM parameters and microwave absorption

of spinel absorbers. As shown in the Raman spectra (Fig. 4), the uncalcined hierarchical  $\text{NiCo}_2\text{O}_4$ – $\text{CoNiO}_2$  hybrids display two distinguishable peaks of carbon in the range of  $1000$ – $2000 \text{ cm}^{-1}$ , one broad peak centered at  $\sim 1370 \text{ cm}^{-1}$  (D band), and one other relatively sharp peak at  $\sim 1578 \text{ cm}^{-1}$  (G band). According to the previous literature studies,<sup>40,41</sup> the D band is a breathing mode of  $\text{A}_{1g}$  symmetry involving phonons near the K zone boundary, which is forbidden in perfect graphite and becomes active in the presence of disorder or finite-size crystals of graphite (nanographite crystals); the G band corresponds to the  $\text{E}_{2g}$  mode due to stretching vibrations of the  $\text{sp}^2$  bond, which can be produced by all  $\text{sp}^2$  sites and not only by graphitic carbon. It can be seen that the value of the intensity ratio of these two bands,  $I_{\text{D}}/I_{\text{G}}$ , is 0.80, much smaller than that (0.92) of pristine carbon materials,<sup>23</sup> which is a hint that carbon components in these composites have a relatively low graphitization degree, which is very consistent with the XRD results.

The Raman spectra of spinel oxides have been predicted and shown to be characterized by five peaks.<sup>42</sup> There are three dominant peaks labeled for spinel  $\text{Co}_3\text{O}_4$ .<sup>43</sup> The high-frequency peak at  $693 \text{ cm}^{-1}$  has been assigned to a vibration largely determined by the octahedral oxygen ions, *i.e.*, octahedral/ $\text{Co}^{3+}$ .<sup>43</sup> As  $\text{Co}^{3+}$  is replaced by  $\text{Ni}^{2+}$ , the peak weakens and shifts to lower frequency due to lower concentration of the octahedral/ $\text{Co}^{3+}$  moiety (see Fig. 4, the bands at  $665$  and  $652 \text{ cm}^{-1}$ ). Also,  $\text{Ni}^{2+}$  substitution at octahedral sites would be expected to induce a significant amount of disorder in the lattice, particularly since the

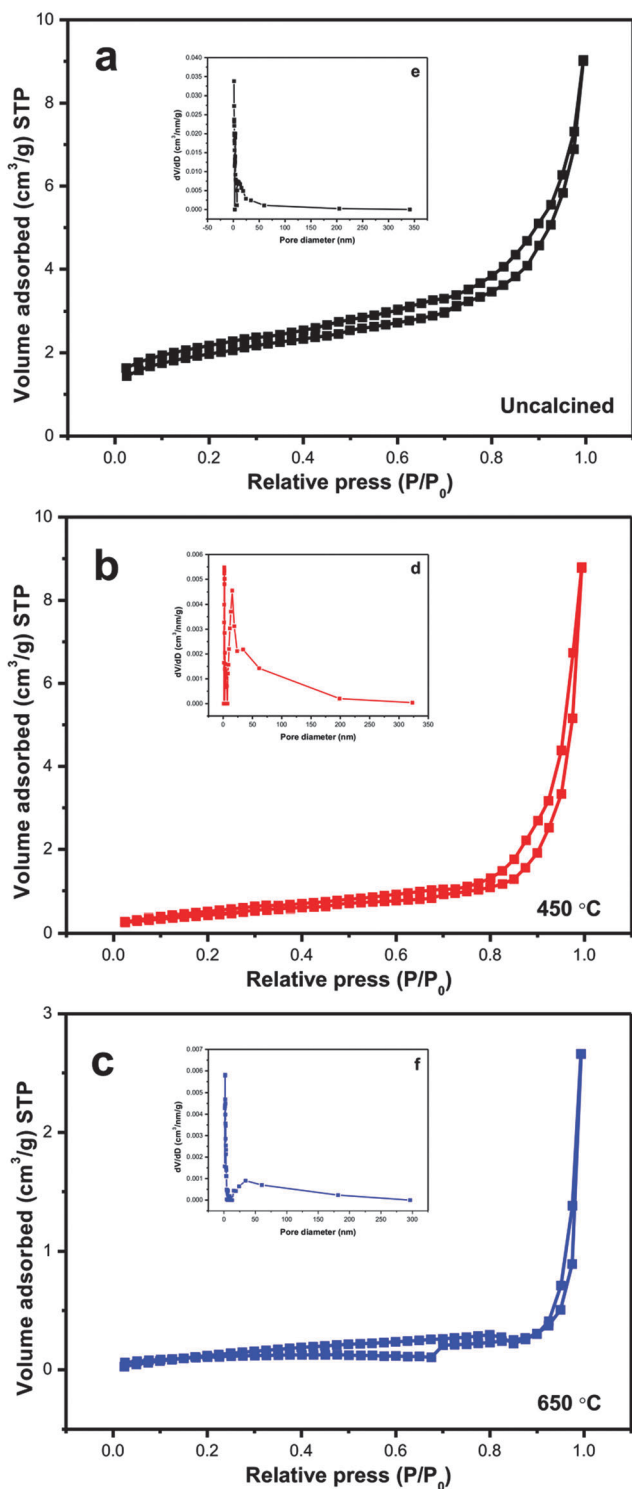


Fig. 3 N<sub>2</sub> adsorption–desorption isotherms and the pore-size distributions (insets) of the hierarchical NiCo<sub>2</sub>O<sub>4</sub>–CoNiO<sub>2</sub> hybrids.

octahedral units share edges.<sup>42,44–46</sup> This disorder would reduce symmetry and promote an even more dramatic reduction (as observed) of the high-frequency Raman band intensity since it arises from a highly symmetric mode. The two lower frequency Raman bands labeled in Fig. 4 are due to combined vibrations of

Table 1 Textural properties of the hierarchical NiCo<sub>2</sub>O<sub>4</sub>–CoNiO<sub>2</sub> hybrids

Samples	Specific surface area (m <sup>2</sup> g <sup>-1</sup> )	Pore volume (cm <sup>3</sup> g <sup>-1</sup> )	Average pore diameter (nm)
Uncalcined	154.84	0.31	8.32
450 °C	36.84	0.20	3.30
650 °C	23.47	0.10	4.33

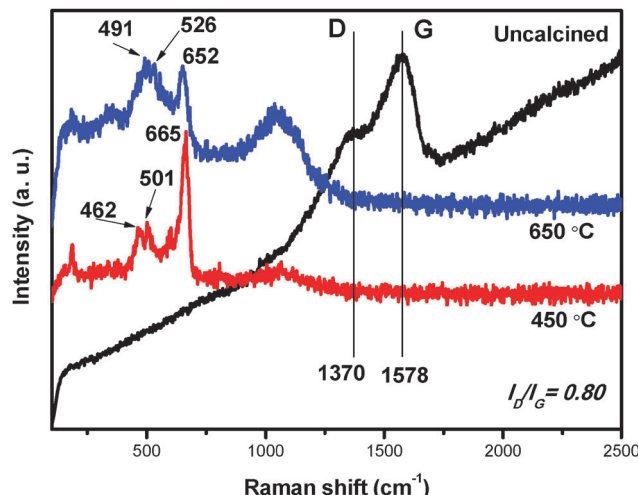
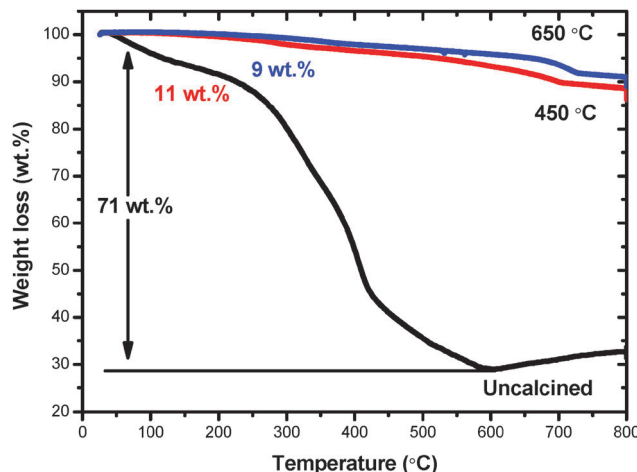


Fig. 4 Raman spectra of the hierarchical NiCo<sub>2</sub>O<sub>4</sub>–CoNiO<sub>2</sub> hybrids.

tetrahedral and octahedral oxygen atoms.<sup>46,47</sup> Their behavior is also as expected: they weaken and broaden with Ni<sup>2+</sup> substitution as the concentration of tetrahedral/Co<sup>2+</sup> (491 and 462 cm<sup>-1</sup>) is diluted and octahedral/Ni<sup>2+</sup> (526 and 501 cm<sup>-1</sup>) forms. It can be inferred that the disorder in the lattice would induce the formation of excess dipole and dipole polarization, which is a benefit for EM wave dissipation and thus results in enhanced microwave absorption properties.

From the thermogravimetric (TG) curve of the uncalcined hierarchical NiCo<sub>2</sub>O<sub>4</sub>–CoNiO<sub>2</sub> hybrid in Fig. 5, one can see two weight losses due to the removal of adsorbed water (about 150 °C) and combustion of carbon (starting at about 250 °C), and one weak weight increase region (transformation of CoNiO<sub>2</sub> to NiCo<sub>2</sub>O<sub>4</sub>) in the temperature range of ~600–800 °C, and the residual weight is about 29 wt% at 600 °C. For calcined hierarchical NiCo<sub>2</sub>O<sub>4</sub>–CoNiO<sub>2</sub> hybrids, the slight mass loss occurs over the whole temperature range (11 wt% and 9 wt% for the samples calcined at 450 °C and 650 °C, respectively), which may be accounted for the transformation of CoNiO<sub>2</sub> to NiCo<sub>2</sub>O<sub>4</sub>. According to the mass loss, we can draw a conclusion that the weight percentage of hierarchical NiCo<sub>2</sub>O<sub>4</sub>–CoNiO<sub>2</sub> hybrids in the uncalcined sample is ~29 wt%.

The more detailed elemental composition and the oxidation state of the hierarchical NiCo<sub>2</sub>O<sub>4</sub>–CoNiO<sub>2</sub> hybrids were further characterized by XPS measurements and the corresponding results are presented in Fig. 6. By using a Gaussian fitting method, the O1s emission spectra of the calcined samples (Fig. 6a) are best fitted with three oxygen contributions, denoted O1 (526.5 eV), O2 (528.9 eV), and O3 (530.4 eV), associating with the typical metal–oxygen bonds,<sup>48</sup> the oxygen in hydroxyl groups,<sup>49</sup> and the

Fig. 5 TG curves of the hierarchical  $\text{NiCo}_2\text{O}_4$ - $\text{CoNiO}_2$  hybrids.

high number of defect sites with low oxygen coordination in the material with a small particle size,<sup>50</sup> respectively. The C1s spectra of all the samples are shown in Fig. 6b to elucidate their surface composition. The peaks centered at 282 eV and 285.9 eV can be attributed to interfacial carbon atoms bonded to hierarchical  $\text{NiCo}_2\text{O}_4$ - $\text{CoNiO}_2$  hybrids or carbon deposited on the surface of hierarchical  $\text{NiCo}_2\text{O}_4$ - $\text{CoNiO}_2$  hybrids and

C-O groups,<sup>51,52</sup> respectively. The above result suggests that hierarchical  $\text{NiCo}_2\text{O}_4$ - $\text{CoNiO}_2$  hybrids have a small distribution of C-O functional groups in the samples.<sup>53</sup> The Co2p spectra shown in Fig. 6c consist of one spin-orbit doublet characteristic of  $\text{Co}^{2+}$  and  $\text{Co}^{3+}$  and two shakeup satellites (identified as "Sat."). Similarly, the Ni2p spectra given in Fig. 6d are composed of one spin-orbit doublet characteristic of  $\text{Ni}^{2+}$  and  $\text{Ni}^{3+}$  and two shakeup satellites. These results show that the surface of the samples has a composition containing  $\text{Co}^{2+}$ ,  $\text{Co}^{3+}$ , and  $\text{Ni}^{2+}$  species. Therefore, the formula of  $\text{NiCo}_2\text{O}_4$ - $\text{CoNiO}_2$  can be generally expressed as follows:  $\text{Co}^{3+}[\text{Co}^{3+}\text{Ni}^{2+}]^{\square}\text{O}_4$ - $\text{Co}^{2+}\text{Ni}^{2+}\text{O}_2$  (the cations within the square bracket are in octahedral sites and the outside ones occupy the tetrahedral sites).<sup>54</sup> In addition, the quantitative analysis of the samples based on the XPS (see Table 2) reveals that the Ni/Co atomic ratios are 0.24, 0.69 and 0.63 for the stoichiometric spinel materials (the theoretical values are 0.5 and 1.0 for  $\text{NiCo}_2\text{O}_4$  and  $\text{CoNiO}_2$ , respectively), indicating large enrichment in Co species (rich  $\text{Co}_3\text{O}_4$  phase) on the surface of the uncalled sample rather than co-existence of hierarchical  $\text{NiCo}_2\text{O}_4$ - $\text{CoNiO}_2$  hybrids in the calcined samples. Actually, the energy-dispersive X-ray (EDX) spectrum of the calcined sample at 450 °C is presented in Fig. S1 (ESI†). The spectrum shows that the atomic ratio of Ni/Co is ~1 in hierarchical  $\text{NiCo}_2\text{O}_4$ - $\text{CoNiO}_2$  hybrids, which is a little higher compared with the XPS results. Furthermore, from Table 2,

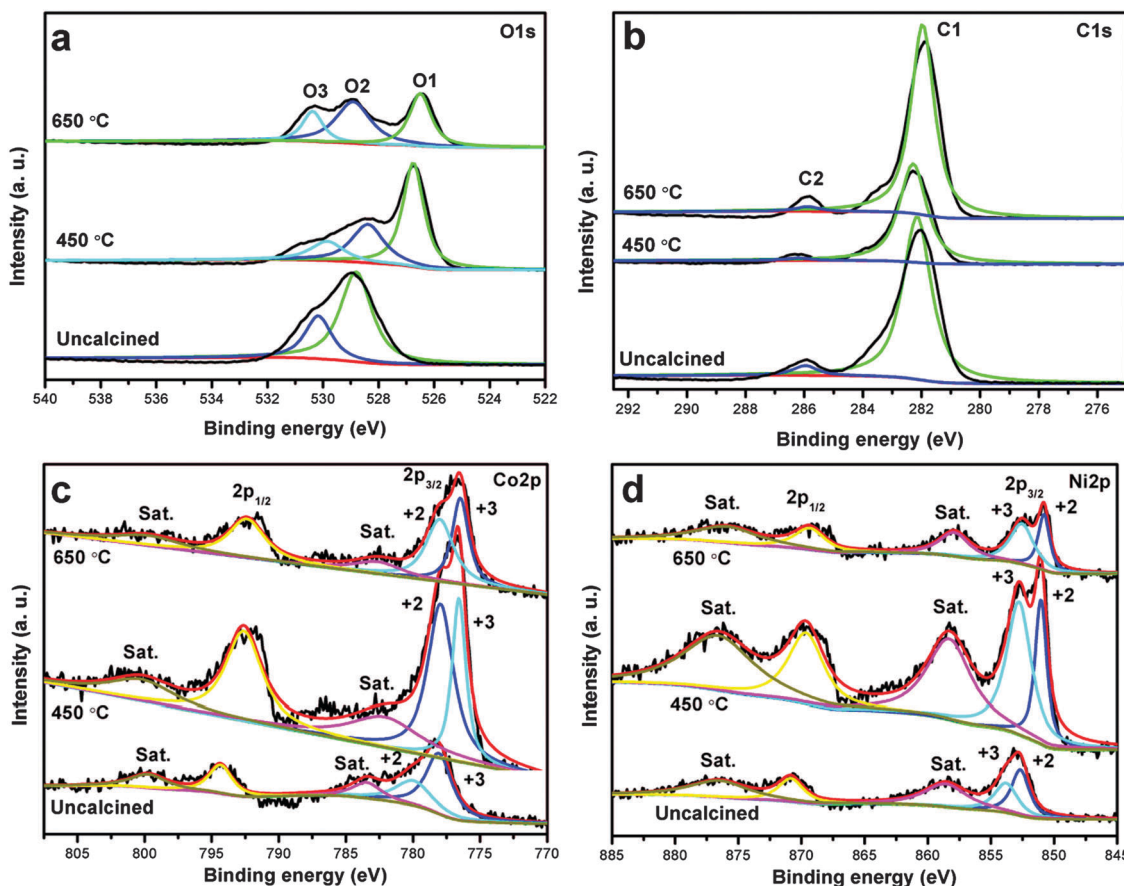
Fig. 6 (a) O1s, (b) C1s, (c) Co2p, and (d) Ni2p spectra of the hierarchical  $\text{NiCo}_2\text{O}_4$ - $\text{CoNiO}_2$  hybrids.

Table 2 Binding energies (eV) and surface atomic ratios of the samples

Samples	Ni2p <sub>3/2</sub>		Co2p <sub>3/2</sub>		Ni/Co (atomic ratio)	Co <sup>2+</sup> /Co <sup>3+</sup> (atomic ratio)
	Ni <sup>2+</sup>	Ni <sup>3+</sup>	Co <sup>3+</sup>	Co <sup>2+</sup>		
Uncalcined	852.7 (54.8%)	853.8 (45.2%)	778.1 (63.0%)	780.0 (37.0%)	0.24	0.59
450 °C	851.0 (34.2%)	852.8 (65.8%)	776.6 (36.2%)	778.0 (63.8%)	0.69	1.76
650 °C	850.8 (40.3%)	852.6 (59.7%)	776.5 (45.4%)	778.0 (54.6%)	0.63	1.20

the Co<sup>2+</sup>/Co<sup>3+</sup> ratio of the calcined samples at 450 °C is 1.76, which suggests that the CoNiO<sub>2</sub>/NiCo<sub>2</sub>O<sub>4</sub> molar ratio is close to 3.52 in hierarchical NiCo<sub>2</sub>O<sub>4</sub>-CoNiO<sub>2</sub> hybrids. Similarly, the Co<sup>2+</sup>/Co<sup>3+</sup> ratio of the calcined sample at 650 °C is close to 1.20. However, the Co<sup>2+</sup>/Co<sup>3+</sup> ratio of the uncalcined sample is 0.59, which is very consistent with the result of pure Co<sub>3</sub>O<sub>4</sub> according to ref. 55. Herein, XPS analysis highlights different cation distributions on the surface of various hierarchical NiCo<sub>2</sub>O<sub>4</sub>-CoNiO<sub>2</sub> hybrids. It can be observed that after calcination at 450 °C the proportion of Co<sup>2+</sup> of the uncalcined sample significantly increases, as the Co<sup>2+</sup>/Co<sup>3+</sup> ratio changed from 0.59 to 1.76. Most of the Co<sup>3+</sup> was reduced by carbon during the heating process (Co<sup>3+</sup> → Co<sup>2+</sup>). However, when the sample was further calcined at 650 °C the amount of Co<sup>2+</sup> decreases due to its oxidation in air at a high temperature (Co<sup>2+</sup>/Co<sup>3+</sup> ratio = 1.20). Compared with the uncalcined sample, the excess of Co<sup>2+</sup> in the calcined hierarchical NiCo<sub>2</sub>O<sub>4</sub>-CoNiO<sub>2</sub> hybrids will definitely induce the disorder in the lattice, which leads to the formation of a high concentration of oxygen vacancies.<sup>55</sup> This surface non-stoichiometry property increases the dipole polarization and interfacial polarization of the materials, which is of benefit for the increase of microwave absorption abilities.

The magnetic properties of the samples were investigated and discussed. Fig. 7 shows the saturation magnetization vs. applied coercivity field ( $M_s$  vs.  $H_c$ ) curves of the samples acquired at a representative temperature of 300 K (inset: enlarged view at low fields). The presence of the NiCo<sub>2</sub>O<sub>4</sub> spinel phase in the samples gives rise to clear hysteresis loops, owing

to its ferromagnetic (FiM) nature. The experimental magnetization has been found to not saturate, even at the maximum applied field (20 kOe), as expected from the contribution of the antiferromagnetic (AFM) phases and magnetic surface disorder effects often observed at reduced dimensions.<sup>56,57</sup> It can be observed that the hierarchical NiCo<sub>2</sub>O<sub>4</sub>-CoNiO<sub>2</sub> hybrid calcined at 450 °C shows an apparent hysteresis loop, the  $H_c$  and  $M_s$  is 211 Oe and 2.40 emu g<sup>-1</sup>, respectively. The calcined hierarchical NiCo<sub>2</sub>O<sub>4</sub>-CoNiO<sub>2</sub> hybrid at 650 °C and the uncalcined one also show the weak hysteresis loops with the parameters of 332 and 830 Oe for  $H_c$ , and 0.57 and 0.75 emu g<sup>-1</sup> for  $M_s$ , respectively.

Importantly, the coercivity exhibits a monotonic behaviour, reaching a value in excess of  $H_c = 830$  Oe for the uncalcined sample (see Fig. 7). Due to the morphology and composition of these materials,  $H_c$  is likely to have two main contributions apart from magnetocrystalline anisotropy: shape anisotropy and AFM-FiM exchange coupling. As the material transforms from nanorods to polyhedral nanocrystals, its shape anisotropy may increase significantly, leading to an increase in coercivity. Moreover, when FiM materials are exchange coupled to AFMs, and the latter has a low anisotropy (like in the case of amorphous NiCo<sub>2</sub>O<sub>4</sub>-CoNiO<sub>2</sub> hybrids), the FiM has to drag the spins of the AFM during the reversal, which costs extra energy, resulting in an increased  $H_c$ . Since this an interface effect, the amount of AFM material and the degree of coupling determine the coercivity enhancement. Moreover, FiM materials are known to have a magnetic disorder at the surface, which depends on the shape that also contributes to  $H_c$  at low temperatures. Cabo *et al.* reported that NiO/NiCo<sub>2</sub>O<sub>4</sub>/Co<sub>3</sub>O<sub>4</sub> composites rich in NiCo<sub>2</sub>O<sub>4</sub> exhibit  $M_s$  in the range of  $M_s = 2\text{--}3.5$  emu g<sup>-1</sup> and moderate coercivities  $H_c = 5\text{--}300$  Oe.<sup>58</sup>

Since the microwave absorption properties of a material is determined by their complex permeability ( $\mu_r = \mu' - j\mu''$ ) and permittivity ( $\epsilon_r = \epsilon' - j\epsilon''$ ), the frequency dependence of complex permeability and permittivity for the hierarchical NiCo<sub>2</sub>O<sub>4</sub>-CoNiO<sub>2</sub> hybrids are measured using a network analyzer and is shown in Fig. 8 and 9. In the whole measurement, the samples were dispersed in a flexible paraffin wax with a concentration of 50 wt%. For the calcined hierarchical NiCo<sub>2</sub>O<sub>4</sub>-CoNiO<sub>2</sub> hybrids at 450 °C and 650 °C, the real part of complex permittivity ( $\epsilon'$ ) decreases from about 18.7 and 6.2 to 14.7 and 4.7, respectively, with the increase of frequency from 2 to 18 GHz, whereas the real part of complex permittivity for the uncalcined sample is almost constant over the whole frequency range with an unobtrusive undulation ( $\epsilon' \approx 3.3$ ). It has to point out that a frequency dispersion behavior in the range of 2–18 GHz exists in our case, that is, their complex

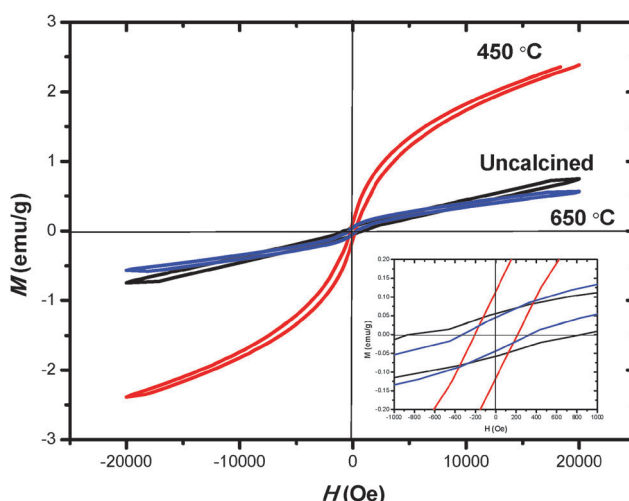


Fig. 7 Magnetic hysteresis loops of the hierarchical NiCo<sub>2</sub>O<sub>4</sub>-CoNiO<sub>2</sub> hybrids.

permittivity will gradually decrease with the increasing frequency. However, it is very interesting that  $\epsilon''$  values in the calcined sample at 450 °C shows a distinguishable frequency-dependence behavior. For example,  $\epsilon''$  values first decrease gradually in the range of 2–10 GHz and then present significant fluctuations with a maximum of 4.3, 5.2 and 5.8 at 10.96 GHz, 14.32 GHz and 16.56 GHz, respectively, with the increasing frequency. For the other two samples,  $\epsilon''$  values decrease slightly from 1.45 to 1.30 and 0.75 to 0.31, respectively. The superior complex permittivity for the calcined sample at 450 °C is attributed to its higher concentration of oxygen vacancies caused by the excess of Co<sup>2+</sup>, which could destroy the balance of the charge distribution and induce dipole polarization and interfacial polarization as well as associated relaxation at the interfaces between NiCo<sub>2</sub>O<sub>4</sub> and CoNiO<sub>2</sub> phases. Through the cooperation of different polarization models and a relaxation process, a large amount of charges can accumulate at the interfaces, especially when the oxygen vacancies possess enough concentration, charge redistribution happens and the density of the electron clouds

in the conjugated area can be easily changed, resulting in the enhanced dielectric loss of the hierarchical NiCo<sub>2</sub>O<sub>4</sub>–CoNiO<sub>2</sub> hybrids.

Fig. 9 shows the  $\mu'$  and  $\mu''$  of all the samples in the frequency range of 2–18 GHz. The calcined sample at 450 °C decreases from 1.01 to 0.72 over the whole frequency range with slight fluctuation. While the  $\mu''$  values first decrease from 1.22 to 0.01 at 2–10 GHz and then keep almost constant with the increasing frequency. It can be seen that complex permeability of the calcined sample at 450 °C displays the same trend as that of the other two samples. The calcined sample at 450 °C exhibits lower  $\mu'$  values at relatively low frequencies, particularly in the range of 2–10 GHz, whereas higher  $\mu''$  values are distinguished over 2–10 GHz. In comparison with the uncalcined and calcined samples at 650 °C, the enhancement of  $\mu''$  for the calcined sample at 450 °C is mainly due to its ferromagnetic resonance bands located at 2–6 GHz.<sup>11</sup> These ferromagnetic resonances are believed to be related to the natural resonances of these materials.

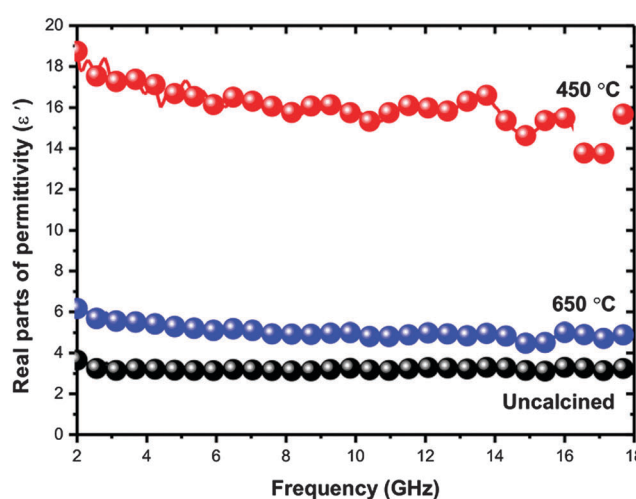


Fig. 8 The frequency dependence of complex permittivity for the hierarchical NiCo<sub>2</sub>O<sub>4</sub>–CoNiO<sub>2</sub> hybrids.

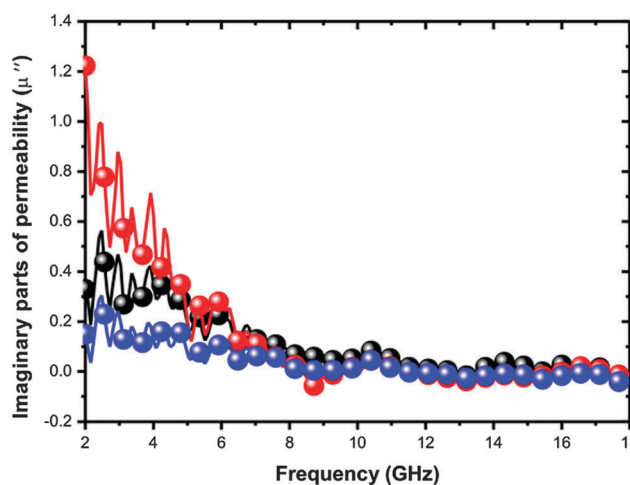
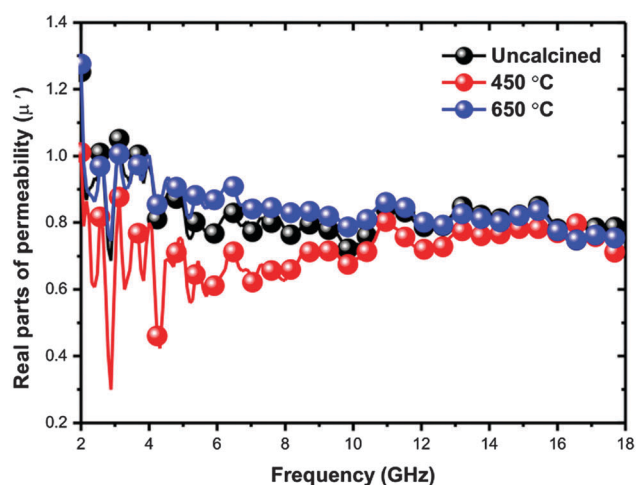
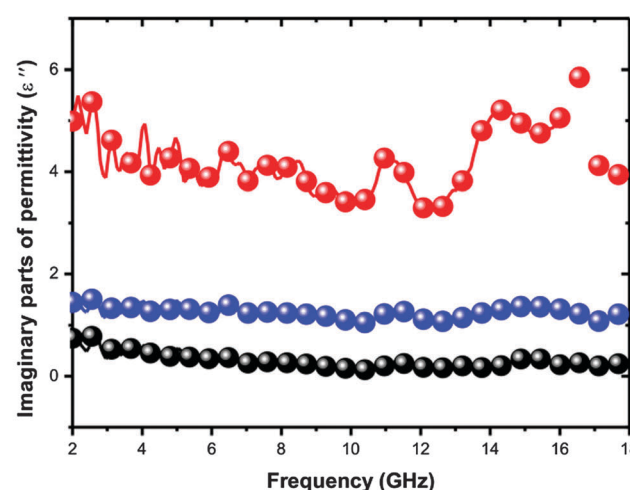


Fig. 9 The frequency dependence of complex permeability for the hierarchical NiCo<sub>2</sub>O<sub>4</sub>–CoNiO<sub>2</sub> hybrids.

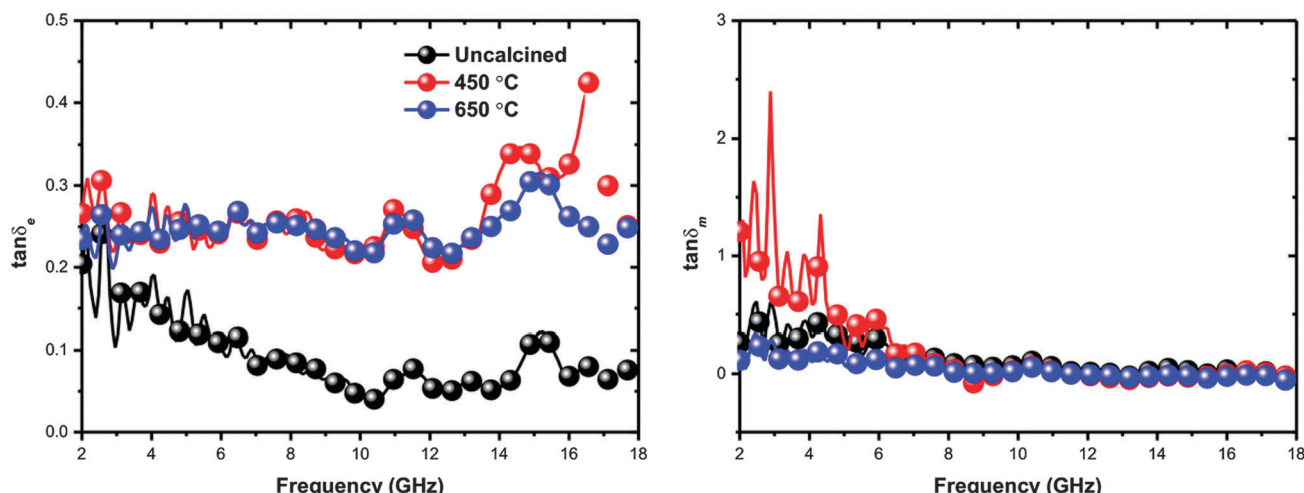


Fig. 10 The frequency dependence of dielectric loss tangent and magnetic loss tangent for the hierarchical  $\text{NiCo}_2\text{O}_4\text{-CoNiO}_2$  hybrids.

Moreover, the frequency dependence of dissipation factors represented by the magnetic loss tangent ( $\tan \delta_m = \mu''/\mu'$ ) and dielectric loss tangent ( $\tan \delta_e = \epsilon''/\epsilon'$ ) for the three samples are displayed in Fig. 10. The values of  $\tan \delta_e$  for the calcined sample at 450 °C are obviously improved in the frequency range of 13–18 GHz, which indicates that the hierarchical  $\text{NiCo}_2\text{O}_4\text{-CoNiO}_2$  hybrids may generate many defects at the interfaces, resulting in high  $\epsilon''$  and improved dielectric loss. In the middle- and high-frequency range (6–18 GHz), the values of  $\tan \delta_e$  are obviously larger than those of  $\tan \delta_m$ , which indicates that the dielectric loss plays a key role in the enhanced absorption properties of the hierarchical  $\text{NiCo}_2\text{O}_4\text{-CoNiO}_2$  hybrids. Furthermore, the dielectric loss may also be caused by dipole polarization and interfacial polarization at microwave frequencies.<sup>2,11</sup> Besides the above-mentioned defect mechanism, the hierarchical  $\text{NiCo}_2\text{O}_4\text{-CoNiO}_2$  hybrids have numerous surface atoms with local breaking of symmetry due to the surface effect as the size decreases to nanoscale (the typical diameter and length of these nanorods are ~10–20 nm and ~200–300 nm, respectively), causing dipoles and dipole polarization. Furthermore, the well dispersed  $\text{NiCo}_2\text{O}_4\text{-CoNiO}_2$  hybrid nanocrystals anchored uniformly on the surface of microspheres, and  $\text{CoNiO}_2$  phase adhered to  $\text{NiCo}_2\text{O}_4$  nanorods may introduce extra interfaces, leading to interfacial polarization and stronger associated relaxation occurring at both hierarchical  $\text{NiCo}_2\text{O}_4\text{-CoNiO}_2$  hybrids-microsphere and  $\text{CoNiO}_2\text{-NiCo}_2\text{O}_4$  interfaces. These polarization effects may also contribute to an increase of the dielectric loss.

In view of the novel nanostructure and remarkable complex permittivity properties of the hierarchical  $\text{NiCo}_2\text{O}_4\text{-CoNiO}_2$  hybrids, the microwave absorption behaviors of the samples were investigated. The physical model for the interaction of microwave and absorber is briefly described below. When the microwave is incident on the absorber backed by a metal plate, the incident microwave is mostly consumed by the absorber through EM wave loss mechanisms. The dominant loss of the incident microwave is the absorption mechanism, in which the energy consumption is owing to the magnetic and dielectric

loss. The magnetic loss is attributed to the natural resonance loss of the magnetic hierarchical  $\text{NiCo}_2\text{O}_4\text{-CoNiO}_2$  hybrids. The dielectric loss is mainly due to the dipole polarization and interfacial polarization of the dielectric hierarchical  $\text{NiCo}_2\text{O}_4\text{-CoNiO}_2$  hybrids.

Typically, the reflection loss (RL) value is used to evaluate the microwave absorption efficiency of absorbers, for example, the RL value of −10 dB is comparable to 90% of microwave absorption. The RL values of an absorber backed by a metal plate were calculated according to the transmit line theory, which is based on the measured complex permittivity and permeability at a given absorber thickness and frequency by the following equation:<sup>37–39</sup>

$$\text{RL} = 20 \log \left| \frac{Z_{\text{in}} - Z_0}{Z_{\text{in}} + Z_0} \right| \quad (1)$$

$$Z_{\text{in}} = Z_0 \left( \frac{\mu_r}{\epsilon_r} \right)^{1/2} \tanh \left\{ j \left( \frac{2\pi f d}{c} \right) (\mu_r \epsilon_r)^{1/2} \right\} \quad (2)$$

where  $Z_{\text{in}}$  is the input impedance of the absorber,  $Z_0$  is the impedance of air,  $f$  is the frequency of an electromagnetic wave,  $d$  is the thickness of a microwave absorber and  $c$  is the velocity of light in a vacuum.

Fig. 11 shows the variations of the RL values *vs.* frequency for the three samples at different thicknesses. The RL values for the uncalcined and calcined samples at 650 °C (Fig. 11a and c) cannot reach −20 dB (99% microwave absorption) within the thickness of 1.0–5.0 mm, indicating that both samples could hardly be used for practical applications. It is clear that the absorption peaks for the calcined sample at 450 °C shift toward a low frequency region as the absorber thickness increases from 1.0 to 5.0 mm. The RL values less than −10 dB and −20 dB are found in the relatively wide frequency bandwidth of 3.92 GHz and 1.36 GHz with the thickness of only 1.55 mm, moreover, an optimal RL value of −42.13 dB is achieved at 11.84 GHz. The results suggest that the calcined hierarchical  $\text{NiCo}_2\text{O}_4\text{-CoNiO}_2$  hybrids at 450 °C have effective absorbing characteristics in wide frequency bands, which is of great interest for the military radar.

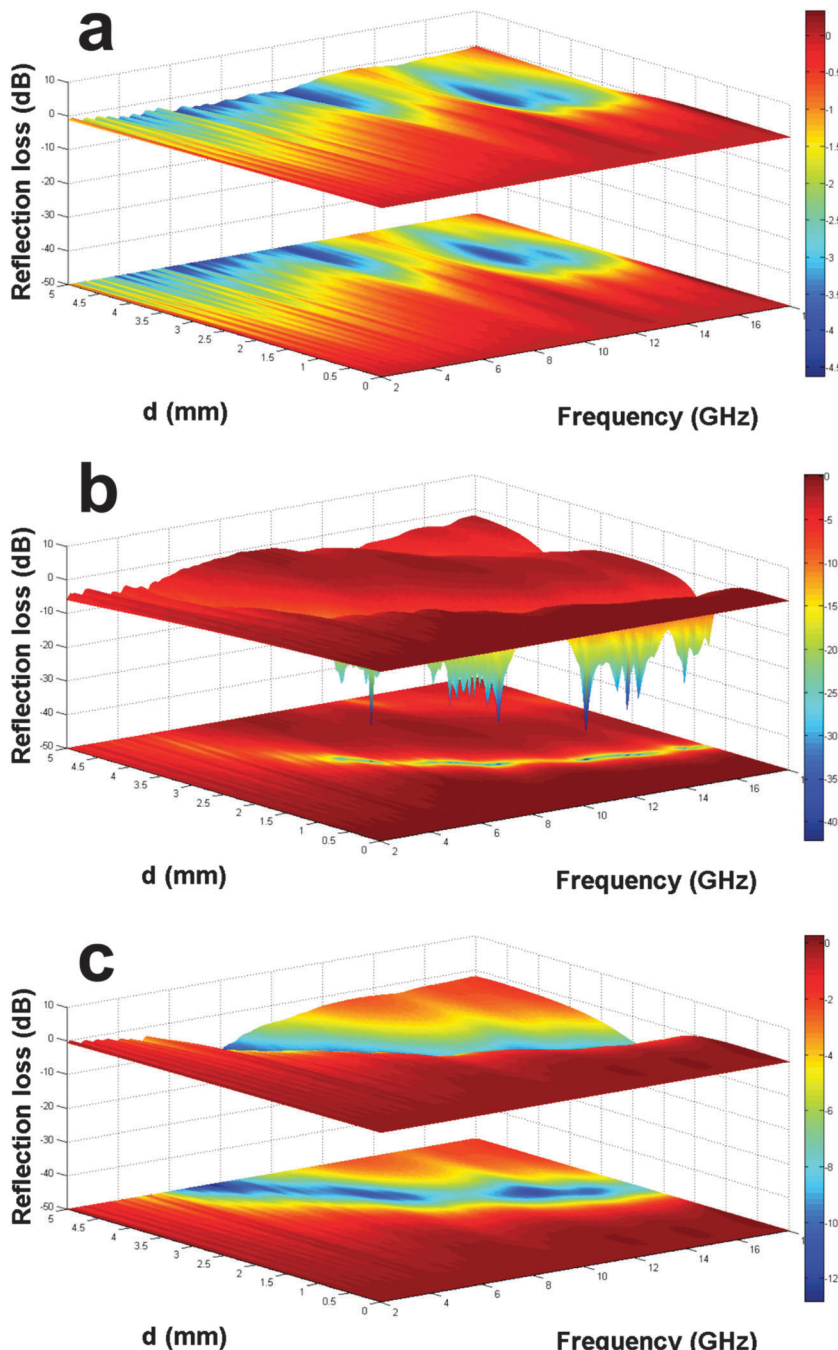


**Fig. 11** Three-dimensional representation of RL values for the paraffin wax composites (50 wt%): (a) uncalcined sample, (b) calcined sample at 450 °C, and (c) calcined sample at 650 °C.

The absorber thickness is one of the critical parameters which determines the intensity and position of the maximum RL. To investigate the physical phenomenon, the quarter-wavelength matching model ( $\lambda/4$ ) was adopted, in which the maximum RL can be achieved at a certain frequency if the absorber thickness satisfies the following equation:<sup>59–63</sup>

$$t_m = n\lambda/4 = nc/(4f_m\sqrt{|\mu_r||\epsilon_r|}) \quad (n = 1, 3, 5, \dots) \quad (3)$$

where  $t_m$  is the thickness of the absorber,  $\lambda$  is the wavelength of the electromagnetic wave,  $f_m$  is the peak frequency of the maximum RL,  $|\mu_r|$  and  $|\epsilon_r|$  are, respectively, the modulus of the measured  $\mu_r$  and  $\epsilon_r$  at  $f_m$ , and  $c$  is the velocity of light in a vacuum. According to the quarter-wavelength matching conditions, when the absorber thickness satisfies eqn (3), the two emerging reflected electromagnetic waves from the air-absorber interface and absorber–metal interface are out of phase by 180°, leading to an extinction of them on the air-absorber interface.

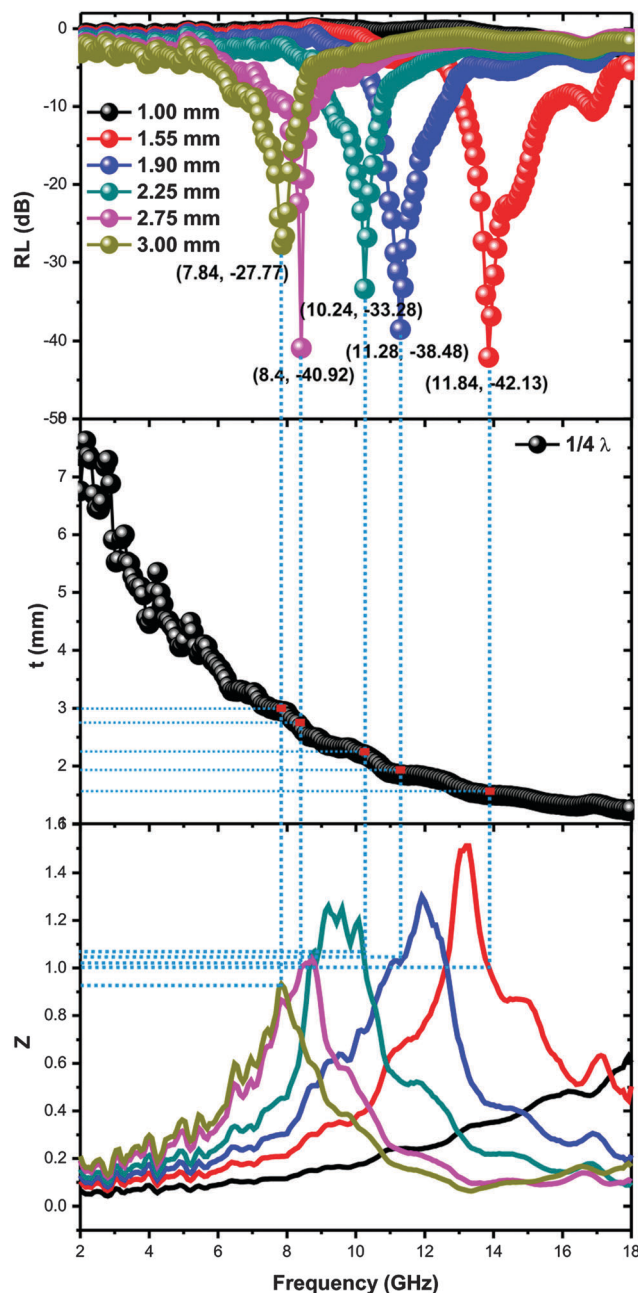


Fig. 12 The frequency dependence of RL values for the calcined sample at 450 °C; simulations of the absorber thickness vs. peak frequency for the calcined sample at 450 °C under  $\lambda/4$  conditions; the modulus of normalized input impedance ( $|Z_{in}/Z_0|$ ) for the calcined sample at 450 °C.

Fig. 12 reveals the variations of RL curves vs. frequency of the calcined hierarchical  $\text{NiCo}_2\text{O}_4$ – $\text{CoNiO}_2$  hybrids at 450 °C. Based on the quarter-wavelength model, a simulation of the thickness ( $t_m$ ) vs. peak frequency ( $f_m$ ) for the sample is displayed. The red symbols are the matching thickness vs. the peak frequency, which were directly extracted from the RL curves above. Obviously, all the red symbols are exactly located around the  $\lambda/4$  curve, which suggests that the relationship between matching thickness and peak frequency for the EM wave absorption of the calcined  $\text{NiCo}_2\text{O}_4$ – $\text{CoNiO}_2$

hybrids at 450 °C obeys the quarter-wavelength matching conditions.

Impedance matching characteristic ( $|Z_{in}/Z_0| = |\mu_r/\epsilon_r|^{1/2} \tanh\{j(2\pi f d/c)(\mu_r\epsilon_r)^{1/2}\}$ ) is also an important parameter for EM wave absorption.<sup>11,64,65</sup> The impedance characteristic of the absorber should approach that of free space, resulting in zero reflection at the air-absorber interface. The frequency dependence of  $Z = |Z_{in}/Z_0|$  for the calcined  $\text{NiCo}_2\text{O}_4$ – $\text{CoNiO}_2$  hybrids at 450 °C is obtained as shown in Fig. 12, below, in which the relationship between peak frequency and  $Z$  at the matching thickness is indicated by the dashed lines. When the matching frequency is 11.84 GHz, the minimum RL can be obtained in Fig. 12 and the relevant  $Z$  is mostly close to 1; furthermore the matching thickness is 1.55 mm on the  $\lambda/4$  curve. Such enhanced absorption properties of the calcined  $\text{NiCo}_2\text{O}_4$ – $\text{CoNiO}_2$  hybrids at 450 °C are ascribed to the combined contribution from their impedance matching characteristics and quarter-wavelength interference performance.

Fig. 13 shows the minimum RL value for the calcined sample at 450 °C is measured to be  $-42.13$  dB at 11.84 GHz. The lowest RL of the calcined sample at 650 °C is  $-12.83$  dB at 7.68 GHz. The uncalcined sample has the worst EM absorption with the minimum RL value being  $-4.59$  dB at 6.80 GHz. The order of the EM absorption for the three samples is ranked as follows: sample-450 °C > sample-650 °C > uncalcined sample.

The EM absorption performance of the hierarchical  $\text{NiCo}_2\text{O}_4$ – $\text{CoNiO}_2$  hybrids shows dependence on the  $\text{Co}^{2+}/\text{Co}^{3+}$  ratio. As shown in Fig. 13, the calcined  $\text{CoNiO}_2$ – $\text{NiCo}_2\text{O}_4$  hybrid at 450 °C with the highest  $\text{Co}^{2+}/\text{Co}^{3+}$  ratio (1.76) endows the material with the best EM absorption performance. A plenty of oxygen defects are formed in the calcined hierarchical  $\text{NiCo}_2\text{O}_4$ – $\text{CoNiO}_2$  hybrids at 450 °C, which could destroy the balance of the charge distribution and induce dipole polarization and associated relaxation. The dipole moment is induced, which is proportional to the defect concentration in the hierarchical  $\text{NiCo}_2\text{O}_4$ – $\text{CoNiO}_2$  hybrids. The increased defect density will lead to enhanced dipole moments. Under the altering EM field, the enhanced dipole polarization can magnify energy dissipation,

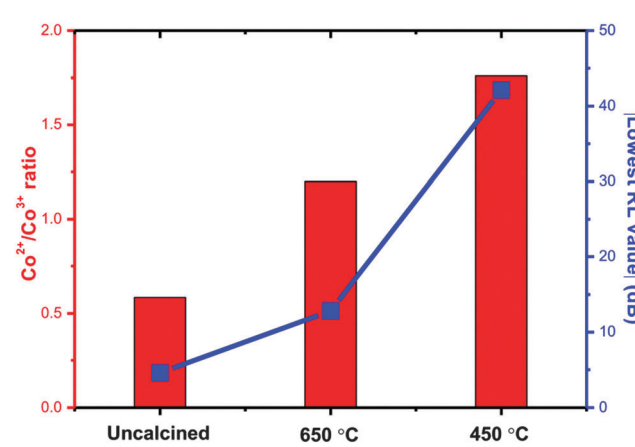


Fig. 13 The relationship between the  $\text{Co}^{2+}/\text{Co}^{3+}$  ratio and the absolute lowest RL value.

**Table 3** EM absorption of some representative spinel absorbers

Samples	Minimum RL value (dB)	Frequency coverage (GHz) (RL < -10 dB)	Thickness (mm)	Percentage (wt%)	Matrix	Ref.
NiCo <sub>2</sub> O <sub>4</sub>	-35.76	4.18	1.50	50	Paraffin	36
NiFe <sub>2</sub> O <sub>4</sub>	-22.5	~1.5	3.00	25	Paraffin	25
NiFe <sub>2</sub> O <sub>4</sub>	-24	4.5	3.50	25	Paraffin	26
CoFe <sub>2</sub> O <sub>4</sub> /GP	-18.5	3.70	2.00	60	Paraffin	27
RGO–MnFe <sub>2</sub> O <sub>4</sub> /PVF	-29.0	4.88	3.00	5	Paraffin	3
NiFe <sub>2</sub> O <sub>4</sub> /GP	-29.2	4.40	2.00	60	Paraffin	28
NiCo <sub>2</sub> O <sub>4</sub> –CoNiO <sub>2</sub>	-42.13	3.92	1.55	50	Paraffin	This work

resulting in the increase of the EM wave absorption ability. On the other hand, the electrons confined at the CoNiO<sub>2</sub>/NiCo<sub>2</sub>O<sub>4</sub> interfaces can move freely along the interfacial planes. The assembled movements of collective interfacial dipoles at the interfaces could enhance the EM absorption ability. Moreover, the calcined hierarchical NiCo<sub>2</sub>O<sub>4</sub>–CoNiO<sub>2</sub> hybrids at 450 °C have special geometrical morphology as described in Fig. 2g. Such isotropic antenna-like structures may be available for the EM wave to penetrate the hybrids and the energy will be induced into dissipative current by random distributed isotropic antennas, and then part of the current will be consumed in the discontinuous networks. Besides, the multi-interfaces between the isotropic antenna frame, matrix, and air bubbles can benefit for the microwave absorption.<sup>66</sup> As a result, the calcined NiCo<sub>2</sub>O<sub>4</sub>–CoNiO<sub>2</sub> hybrids at 450 °C of the most defect content possess the best EM wave absorption ability among the three samples. Table 3 lists the results obtained in the literature for the spinel or spinel/GP absorbers. Compared with the reported spinel or spinel/GP materials, although the effective absorption coverage is not distinguished, the NiCo<sub>2</sub>O<sub>4</sub>–CoNiO<sub>2</sub> absorber has a relatively stronger RL value and thinner thickness. Besides, due to the facile and reliable synthetic method of the NiCo<sub>2</sub>O<sub>4</sub>–CoNiO<sub>2</sub> absorber, the developed material has a great potential to find practical application as an EM wave absorber.

## 4. Conclusions

In summary, we successfully fabricated the amorphous hierarchical NiCo<sub>2</sub>O<sub>4</sub>–CoNiO<sub>2</sub> hybrids by a facile one-pot hydrothermal route. These amorphous hierarchical NiCo<sub>2</sub>O<sub>4</sub>–CoNiO<sub>2</sub> hybrids could be further converted into urchin-like structured NiCo<sub>2</sub>O<sub>4</sub>–CoNiO<sub>2</sub> nanorods and irregular-shaped hierarchical NiCo<sub>2</sub>O<sub>4</sub>–CoNiO<sub>2</sub> polyhedral nanocrystals through air-annealing treatment at 450 °C and 650 °C, respectively. Experimental data indicate that both calcined hierarchical NiCo<sub>2</sub>O<sub>4</sub>–CoNiO<sub>2</sub> hybrids show the improved microwave absorption properties, which is ascribed to the synergistic effect of dielectric CoNiO<sub>2</sub> and NiCo<sub>2</sub>O<sub>4</sub> phases. In particular, calcined hierarchical NiCo<sub>2</sub>O<sub>4</sub>–CoNiO<sub>2</sub> hybrids at 450 °C exhibited a significant enhancement in complex permittivity with respect to other two samples due to their remarkable dipole polarization and interfacial polarization of the dielectric hierarchical NiCo<sub>2</sub>O<sub>4</sub>–CoNiO<sub>2</sub> hybrids. As a result, the calcined hierarchical NiCo<sub>2</sub>O<sub>4</sub>–CoNiO<sub>2</sub> hybrids at 450 °C exhibited a minimum RL value of -42.13 dB at 11.84 GHz with a matching thickness of 1.55 mm and a relatively broad bandwidth (RL ≤ -10 dB) in the 13.12–17.04 GHz range. Very interestingly,

the EM wave absorption performance of the hierarchical NiCo<sub>2</sub>O<sub>4</sub>–CoNiO<sub>2</sub> hybrids shows dependence on the Co<sup>2+</sup>/Co<sup>3+</sup> ratio. The calcined NiCo<sub>2</sub>O<sub>4</sub>–CoNiO<sub>2</sub> hybrids at 450 °C of the most defect concentration possess the best EM wave absorption ability among the samples. Considering the facile approach and high stability of the hierarchical NiCo<sub>2</sub>O<sub>4</sub>–CoNiO<sub>2</sub> hybrids, the present research also opens up the opportunities to fabricate other functional hierarchical spinel hybrids for various industrial applications such as energy conversion, lithium ion batteries, catalysis and electromagnetic shielding materials.

## Acknowledgements

Financial support was provided by National Natural Science Foundation of China (No. 50771082 and 60776822), the Excellent Doctorate Foundation, Doctorate Foundation, and Graduate Starting Seed Fund of Northwestern Polytechnical University, and the Scholarship Award for Excellent Doctoral Student granted by Ministry of Education in China. G.W. thanks the National Natural Science Foundation of China (No. 51407134) and China Postdoctoral Science Foundation (No. 2014M562412).

## References

- 1 R. C. Che, L. M. Peng, X. F. Duan, Q. Chen and X. L. Liang, *Adv. Mater.*, 2004, **16**, 401.
- 2 B. Wen, M. S. Cao, M. M. Lu, W. Q. Cao, H. L. Shi, J. Liu, X. X. Wang, H. B. Jin, X. Y. Fang, W. Z. Wang and J. Yuan, *Adv. Mater.*, 2014, **26**, 3484.
- 3 X. J. Zhang, G. S. Wang, W. Q. Cao, Y. Z. Wei, J. F. Liang, L. Guo and M. S. Cao, *ACS Appl. Mater. Interfaces*, 2014, **6**, 7471.
- 4 Y. L. Ren, H. Y. Wu, M. M. Lu, Y. J. Chen, C. L. Zhu, P. Gao, M. S. Cao, C. Y. Li and Q. Y. Ouyang, *ACS Appl. Mater. Interfaces*, 2012, **4**, 6436.
- 5 J. L. Xie, M. G. Han, L. Chen, R. X. Kuang and L. J. Deng, *J. Magn. Magn. Mater.*, 2007, **314**, 37.
- 6 L. B. Kong, Z. W. Li, L. Liu, R. Huang, M. Abshinova, Z. H. Yang, C. B. Tang, P. K. Tan, C. R. Deng and S. Matitsine, *Int. Mater. Rev.*, 2013, **58**, 203.
- 7 Y. C. Qing, D. D. Min, Y. Y. Zhou, F. Luo and W. C. Zhou, *Carbon*, 2015, **86**, 98.
- 8 Y. C. Qing, W. C. Zhou, F. Luo and D. M. Zhu, *J. Magn. Magn. Mater.*, 2009, **321**, 25.
- 9 G. H. Pan, J. Zhu, S. L. Ma, G. B. Sun and X. J. Yang, *ACS Appl. Mater. Interfaces*, 2013, **5**, 12716.

- 10 G. B. Sun, B. X. Dong, M. H. Cao, B. Q. Wei and C. W. Hu, *Chem. Mater.*, 2011, **23**, 1587.
- 11 X. H. Li, J. Feng, Y. P. Du, J. T. Bai, H. M. Fan, H. L. Zhang, Y. Peng and F. S. Li, *J. Mater. Chem. A*, 2015, **3**, 5535.
- 12 G. X. Tong, F. T. Liu, W. H. Wu, F. F. Du and J. G. Guan, *J. Mater. Chem. A*, 2014, **2**, 7373.
- 13 X. A. Fan, J. G. Guan, Z. Z. Li, F. Z. Mou, G. X. Tong and W. Wang, *J. Mater. Chem.*, 2010, **20**, 1676.
- 14 X. W. Yin, L. Kong, L. T. Zhang, L. F. Cheng, N. Travitzky and P. Greil, *Int. Mater. Rev.*, 2014, **59**, 326.
- 15 M. K. Han, X. W. Yin, L. Kong, M. Li, W. Y. Duan, L. T. Zhang and L. F. Cheng, *J. Mater. Chem. A*, 2014, **2**, 16403.
- 16 Y. F. Zhu, L. Zhang, T. Natsuki, Y. Q. Fu and Q. Q. Ni, *ACS Appl. Mater. Interfaces*, 2014, **4**, 2101.
- 17 G. Z. Wang, Z. Gao, S. W. Tang, C. Q. Chen, F. F. Duan, S. C. Zhao, S. W. Lin, Y. H. Feng, L. Zhou and Y. Qin, *ACS Nano*, 2012, **6**, 11009.
- 18 H. Zhou, J. C. Wang, J. D. Zhuang and Q. Liu, *Nanoscale*, 2013, **5**, 12502.
- 19 X. Sun, J. P. He, G. X. Li, J. Tang, T. Wang, Y. X. Guo and H. R. Xue, *J. Mater. Chem. C*, 2013, **1**, 765.
- 20 Y. Shen, Y. H. Lin and C. W. Nan, *Adv. Funct. Mater.*, 2007, **17**, 2405.
- 21 H. T. Liu, H. F. Cheng, Z. Y. Chu and D. Y. Zhang, *Mater. Des.*, 2007, **28**, 2166.
- 22 S. Gu, J. P. Barrett, T. H. Hand, B. I. Popa and S. A. Cummer, *J. Appl. Phys.*, 2010, **108**, 064913.
- 23 Y. C. Du, W. W. Liu, R. Qiang, Y. Wang, X. J. Han, J. Ma and P. Xu, *ACS Appl. Mater. Interfaces*, 2014, **6**, 12997.
- 24 J. Y. Dong, R. Ullal, J. Han, S. H. Wei, X. Ouyang, J. Z. Dong and W. Gao, *J. Mater. Chem. A*, 2015, **3**, 5285.
- 25 X. Gu, W. M. Zhu, C. J. Jia, R. Zhao, W. Schmidt and Y. Q. Wang, *Chem. Commun.*, 2011, **47**, 5337.
- 26 W. M. Zhu, L. Wang, R. Zhao, J. W. Ren, G. Z. Lu and Y. Q. Wang, *Nanoscale*, 2011, **3**, 2862.
- 27 M. Fu, Q. Z. Jiao, Y. Zhao and H. S. Li, *J. Mater. Chem. A*, 2014, **2**, 735.
- 28 M. Fu, Q. Z. Jiao and Y. Zhao, *J. Mater. Chem. A*, 2013, **1**, 5577.
- 29 P. B. Liu, Y. Huang and X. Sun, *ACS Appl. Mater. Interfaces*, 2013, **5**, 12355.
- 30 Y. J. Chen, Z. Y. Lei, H. Y. Wu, C. L. Zhu, P. Gao, Q. Y. Ouyang, L. H. Qi and W. Qin, *Mater. Res. Bull.*, 2013, **48**, 3362.
- 31 D. Z. Chen, G. S. Wang, S. He, J. Liu, L. Guo and M. S. Cao, *J. Mater. Chem. A*, 2013, **1**, 5996.
- 32 T. S. Wang, Z. H. Liu, M. M. Lu, B. Wen, Q. Y. Ouyang, Y. J. Chen, C. L. Zhu, P. Gao, C. Y. Li, M. S. Cao and L. H. Qi, *J. Appl. Phys.*, 2013, **113**, 024314.
- 33 D. R. Rolison, J. W. Long, J. C. Lytle, A. E. Fischer, C. P. Rhodes, T. M. McEvoy, M. E. Bourg and A. M. Lubers, *Chem. Soc. Rev.*, 2009, **38**, 226.
- 34 A. J. Mieszawska, R. Jalilian, G. U. Sumanasekera and F. P. Zamborini, *Small*, 2007, **3**, 722.
- 35 H. Y. Sun, Y. L. Yu, J. Luo, M. Ahmad and J. Zhu, *CrystEngComm*, 2012, **14**, 8626.
- 36 J. Zhan, Y. L. Yao, C. F. Zhang and C. J. Li, *J. Alloys Compd.*, 2014, **585**, 240.
- 37 H. J. Wu, G. L. Wu and L. D. Wang, *Powder Technol.*, 2015, **269**, 443.
- 38 H. J. Wu, G. L. Wu, Q. F. Wu and L. D. Wang, *Mater. Charact.*, 2014, **97**, 18.
- 39 H. J. Wu, Q. F. Wu and L. D. Wang, *Mater. Charact.*, 2015, **103**, 1.
- 40 R. J. Nemanich and S. A. Solin, *Phys. Rev. B: Condens. Matter Mater. Phys.*, 1979, **20**, 392.
- 41 R. O. Dillon, J. A. Woollam and V. Ketkanant, *Phys. Rev. B: Condens. Matter Mater. Phys.*, 1984, **29**, 3482.
- 42 J. Preudhomme and P. Tarte, *Spectrochim. Acta, Part A*, 1971, **27**, 961.
- 43 C. F. Windisch Jr., G. J. Exarhos and R. R. Owings, *J. Appl. Phys.*, 2004, **95**, 5435.
- 44 C. F. Windisch Jr., G. J. Exarhos, K. F. Ferris, M. H. Engelhard and D. C. Stewart, *Thin Solid Films*, 2001, **398–399**, 45.
- 45 C. F. Windisch Jr., K. F. Ferris, G. J. Exarhos and S. K. Sharma, *Thin Solid Films*, 2002, **420–421**, 89.
- 46 C. F. Windisch Jr., G. J. Exarhos and S. K. Sharma, *J. Appl. Phys.*, 2002, **92**, 5572.
- 47 L. C. Schumacher and I. B. Holzhueter, *Electrochim. Acta*, 1990, **35**, 975.
- 48 J. F. Marco, J. R. Gancedo and M. Gracia, *J. Solid State Chem.*, 2000, **153**, 74.
- 49 Y. E. Roginskaya, O. V. Morozova, E. N. Lubnin, Y. E. Ulitina, G. V. Lopukhova and S. Trasatti, *Langmuir*, 1997, **13**, 4621.
- 50 V. M. Jimenez, A. Fernandez, J. P. Espinos and A. R. Gonzalez-Elipe, *J. Electron Spectrosc. Relat. Phenom.*, 1995, **71**, 61.
- 51 R. Larciprete, S. Lizzit, C. Cepek, S. Botti and A. Goldoni, *Surf. Sci.*, 2003, **532–535**, 886.
- 52 X. Chen, A. R. Tadd and J. W. Schwank, *J. Catal.*, 2007, **251**, 374.
- 53 M. M. Titirici, M. Antonietti and A. Thomas, *Chem. Mater.*, 2006, **18**, 3808.
- 54 J. G. Kim, D. L. Pugmire, D. Battaglia and M. A. Langell, *Appl. Surf. Sci.*, 2000, **165**, 70.
- 55 B. Solsona, E. Aylón, R. Murillo, A. M. Mastral, A. Monzonís, S. Agouram, T. E. Davies, S. H. Taylor and T. Garcia, *J. Hazard. Mater.*, 2011, **187**, 544.
- 56 X. Batlle and A. Labarta, *J. Phys. D: Appl. Phys.*, 2002, **35**, R15.
- 57 S. Mørup, D. E. Madsen, C. Frandsen, C. R. Bahl and M. F. Hansen, *J. Phys.: Condens. Matter*, 2007, **19**, 213202.
- 58 M. Cabo, E. Pellicer, E. Rossinyol, M. Estrader, A. López-Ortega, J. Nogués, O. Castell, S. Surinach and M. D. Baró, *J. Mater. Chem.*, 2010, **20**, 7021.
- 59 X. H. Li, J. Feng, H. Zhu, C. H. Qu, J. T. Bai and X. L. Zheng, *RSC Adv.*, 2014, **4**, 33619.
- 60 X. L. Zheng, J. Feng, Y. Zong, H. Miao, X. Y. Hu, J. T. Bai and X. H. Li, *J. Mater. Chem. C*, 2015, **3**, 4452.

- 61 F. S. Wen, F. Zhang and Z. Y. Liu, *J. Phys. Chem. C*, 2011, **115**, 14025.
- 62 X. H. Li, H. B. Yi, J. W. Zhang, J. Feng, F. S. Li, D. S. Xue, H. L. Zhang, Y. Peng and N. J. Mellors, *J. Nanopart. Res.*, 2013, **15**, 1472.
- 63 X. H. Li, X. H. Guo, T. C. Liu, X. L. Zheng and J. T. Bai, *Mater. Res. Bull.*, 2014, **59**, 137.
- 64 Z. J. Wang, L. N. Wu, J. G. Zhou, W. Cai, B. Z. Shen and Z. H. Jiang, *J. Phys. Chem. C*, 2013, **117**, 5446.
- 65 M. S. Cao, R. R. Qin, J. Qiu and J. Zhu, *Mater. Des.*, 2003, **24**, 391.
- 66 Y. J. Chen, G. Xiao, T. S. Wang, Q. Y. Ouyang, L. H. Qi, Y. Ma, P. Gao, C. L. Zhu, M. S. Cao and H. B. Jin, *J. Phys. Chem. C*, 2011, **115**, 13603.